

## Surface Mechanical Attrition Treatment and Corrosion Resistance Behavior of TA2 Anodic Oxide Film

Zhiwen Wang<sup>1,2</sup>, Ruijia Diao<sup>1,2</sup>, Zhentao Yuan<sup>2</sup>, Xiaohua Yu<sup>1,\*</sup>, Tianlin Fu<sup>2</sup>, Yan Zhao<sup>1</sup>, Zhaolin Zhan<sup>2</sup>

<sup>1</sup> National Engineering Research Center of Waste Resource Recovery, Kunming University of Science and Technology, Kunming 650093, China.

<sup>2</sup> Faculty of Materials Science and Engineering, Kunming University of Science and Technology, Kunming 650093, China.

<sup>3</sup> National and Local Joint Engineering Laboratory for Lithium-ion Batteries and Materials Preparation Technology, Key Laboratory of Advanced Battery Materials of Yunnan Province, Faculty of Materials Science and Engineering, Kunming University of Science and Technology, Kunming 650093, China.

\*E-mail: [xiaohua\\_y@163.com](mailto:xiaohua_y@163.com)

Received: 9 January 2018 / Accepted: 2 March 2018 / Published: 10 April 2018

---

A new method of surface mechanical attrition treatment (SMAT) for controlling the microstructure of a film was proposed, and the microstructure as well as the corrosion resistance of the film were investigated. The thickness and elemental distribution of the film were determined via scanning electron microscopy and energy dispersive spectroscopy. The crystallinity and valence state composition of the film were investigated by means of X-ray diffraction, Raman spectroscopy, and X-ray photoelectron spectroscopy. In addition, the corrosion resistance behavior of the film was assessed with an electrochemical workstation. The results revealed that SMAT can increase the growth rate, thickness, compactness, adhesion strength, and stability of the film. Furthermore, this process can yield a reduction in the number of channels for Cl<sup>-</sup> ion transport in the film. The thickness of the film was 3.7 times higher than that of the pre-processed film. Moreover, the self-corrosion potential increased by 36.96% (from -0.441 V to -0.278 V) and the self-corrosion current density decreased by 44.12% (from 0.034 A.cm<sup>-1</sup> to 0.019 A.cm<sup>-1</sup>). This method can serve as an effective treatment that generates films offering excellent protection to titanium and titanium alloys.

---

**Keywords:** TA2 pure titanium; SMAT; anodization; film structure; corrosion resistance behavior

### 1. INTRODUCTION

Titanium (Ti) and Ti alloys have excellent mechanical properties, corrosion resistance, and biocompatibility, and have therefore been widely used in many fields, such as aerospace and biomedicine [1]. However, these materials have high chemical activities, and the naturally formed

oxide film exhibits weak adhesion, has a low density, and can be easily destroyed [2]. Anodization is a cheap and effective electrochemical treatment, which is widely used for the surface treatment of Ti [3]. However, recent studies have shown that improvement of the corrosion resistance is limited, owing to the low thickness of the films produced via this method [4,5].

The mechanism of anodic oxide film formation is manifested via the growth and dissolution of the film during the anodization process. This growth is controlled by the nucleation characteristics and diffusion behavior of the substrate surface. The correlation among the wetting angle, radius of the substrate particles, and radius ratio of the critical embryo has been investigated [6,7]. Fletcher et al. [8] determined the influence of the substrate particle size on the heterogeneous nucleation process on a convex substrate. By introducing the fractional dimension of scaling invariance, Wang et al. [9] showed that a rough surface is super hydrophilic, and (compared with a smooth surface) can provide a greater grain-heterogeneous nucleation density. Moreover, a previous study showed that growth of the oxide film during the anodization process depends on the interdiffusion characteristics of oxygen (O) atoms and vacancies [10]. Yu et al. [11,12] investigated the grain size dependence of the diffusion activation energy and surface energy by using a thermodynamic method. They found that the activation energy decreases with decreasing grain size, whereas the surface energy increases.

Surface mechanical attrition treatment (SMAT) can generate numerous defects such as dislocations, twin crystals, and vacancies on the surface of the substrate. This method represents an effective means of controlling the surface roughness and diffusion activation energy [13,14]. Therefore, in this work, SMAT is proposed as a method of generating an anodic oxide film (with a controlled microstructure) on the surface of pure Ti. The microstructure of this film is investigated via scanning electron microscopy (SEM), energy dispersive spectroscopy (EDS), X-ray diffraction (XRD), and X-ray photoelectron spectroscopy (XPS). The corrosion resistance behavior of the film is investigated using an electrochemical workstation.

## 2. EXPERIMENT

### 2.1 Experimental method

A TA2 pure Ti (dimensions: 100 mm × 100 mm × 2 mm), with composition shown in Table 1, was used as the base material in the experiments.

**Table 1.** Chemical composition of the base material

Element	Fe	C	N	H	O	Ti
Mass fraction/%	0.35	0.17	0.03	0.014	0.33	Bal

1) A metal material surface nanocrystallization test machine (SNC-1) was used to perform SMAT on the Ti plate. The process was performed under the following conditions: projectile material: GCr15, projectile diameter: 8 mm, vibration frequency: 50 Hz, best processing time: 45 min [15]. 2)

The treated samples were cut to sizes of 50 mm × 10 mm × 2 mm. 3) Prior to anodization, the surface oil of the sample was removed via ultrasonic cleaning for 15 min each with acetone, alcohol, and deionized water. 4) Anodization was performed in an electrolyzer. The process was conducted under the following conditions: electrolyte: 0.5 mol/L H<sub>2</sub>SO<sub>4</sub> solution, voltage: 50 V, and electrolysis time: 0.5 h.

## 2.2 Detection Means

The micromorphology of the sample was observed via SEM (LEO 1530Vp Germany) performed at an acceleration voltage of 15 kV; the built-in EDS was used to analyze the elemental content and distribution of the sample cross-section. Furthermore, XRD (D8 ADVANCE Germany; radioactive source: Cu K $\alpha$  (1486.6 eV,  $\lambda = 0.15406$  nm), operating voltage and current: 30 kV and 30 mA, respectively) was used to determine the crystallinity and stability of the oxide film. Moreover, XPS (PHI5000 Versaprobe-II Germany) was used to analyze the element composition and changes in the valence state of the film. The anode was Al target ( $h\nu = 1486.6$  eV).

An electrochemical workstation (PARSTAT 4000) was used to investigate the corrosion resistance behavior of the sample. In the three electrode system, Pt and saturated calomel electrode (SCE) were used as the counter electrode and the reference electrode, respectively. Tests were performed at a temperature of  $27 \pm 0.1$  °C, and a potential scanning rate of 0.03 mV/s. The potentiodynamic polarization test was performed after the sample was soaked for 1 h in a 3.5 wt.% NaCl solution. In addition, the electrochemical impedance spectroscopy (EIS) measurements were performed under open circuit potential. The electrochemical experiments were all repeated five times to ensure the accuracy of the measurement.

## 3. RESULTS AND DISCUSSION

### 3.1 Micromorphology and element composition of the film

The micromorphology and elemental composition of the TA2 (Fig. 1[a]) and SMAT (Fig. 1[b]) samples cross-sections are shown in Fig. 1. The oxide film is composed mainly of Ti and O. Based on the distribution and variation in the Ti and O content, the material can be divided into three zones namely, the: outer layer, transition layer, and inner layer. In the outer zone, the O content is higher than the Ti content and, hence, this layer is considered a dense oxide film structure. The Ti content increases with increasing depth into the film, whereas the O content decreases, thereby resulting in a gradient structure, which may yield increased adhesion strength between the film and the substrate. In the outer zone, Ti/O elements are in a stable state and the O content is almost zero and, hence, the substrate can be considered a pure Ti substrate. From the cross-sectional SEM image, we see that the 425-nm-thick and 1562-nm-thick oxide films are formed on the TA2 and SMAT samples, respectively. The thickness of the oxide film on the SMAT sample is 1137 nm (i.e., 3.7 times) higher than that formed on the TA2 sample.

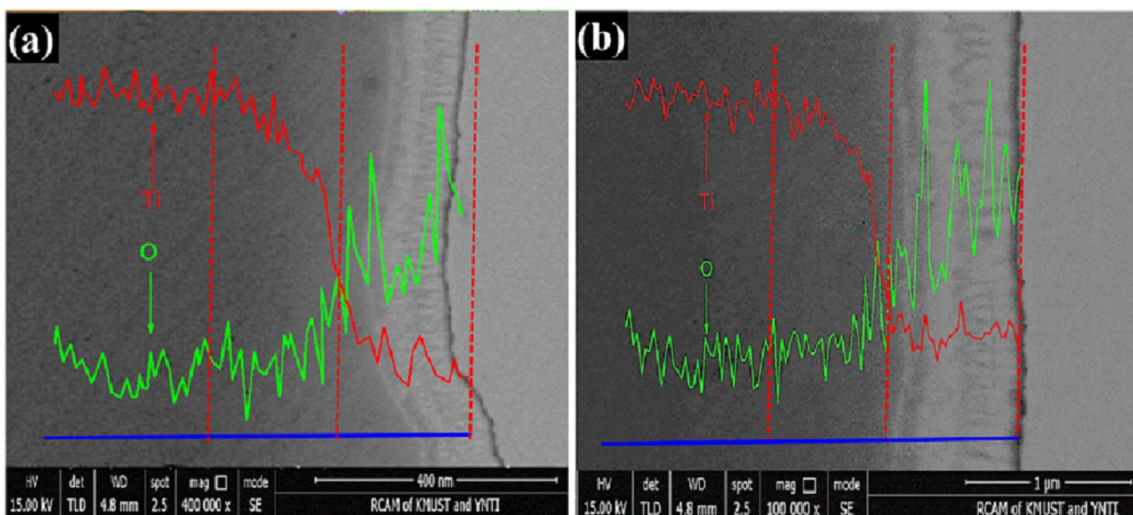


**Figure 1.** Micromorphology and elemental composition of the (a) TA2 and (b) SMAT samples.

According to the Wenzel model [16], the apparent wetting angle of the solution and the substrate, roughness factor of the substrate surface, and intrinsic wetting angle of the solution and the smooth substrate are related as follows:

$$\cos \theta^* = f \cdot \cos \theta \tag{1}$$

where,  $\theta^*$ ,  $f$ , and  $\theta$  are the apparent wetting angle of the rough interface, roughness factor of the substrate interface, and intrinsic wetting angle of the substrate, respectively.

The results showed that  $\theta$  of the natural oxide film on the surface of pure Ti is  $<90^\circ$  and the substrate is hydrophilic [17,18]. Based on equation (1), we see that the apparent wetting angle of the rough interface decreases with increasing surface roughness. The heterogeneous nucleation work on the rough interface [19] is given as follows:

$$\Delta G^* = \left( \frac{16\pi\gamma_{LS}^3}{3\Delta G_V^2} \right) \cdot f(\theta^*)$$

$$f(\theta^*) = \frac{(1 - \cos \theta^*)^2 \cdot (2 + \cos \theta^*)}{4} \tag{2}$$

ere,  $\Delta G^*$ ,  $\gamma_{LS}$ ,  $\Delta G_V$ , and  $f(\theta^*)$  are the heterogeneous nucleation work on the rough interface, Gibbs free energy of the solid liquid interface, free energy difference of unit volume in the solid liquid interface, and the apparent wetting angle function, respectively.

The average roughness ( $R_a$ ) and the Root Mean Square roughness ( $R_{ms}$ ) determined via three-dimensional atomic force microscopy of the TA2 and SMAT samples before anodization. The  $R_a$  of TA2 and SMAT samples before anodization are 37.2 and 49.8, the  $R_{ms}$  are 36.5 and 65.8 respectively. It shows that the surface roughness of the SMAT sample is higher than that of the TA2 sample. The magnitude of the heterogeneous nucleation work on the rough surface varies with the apparent wetting angle of the surface (see equation (2)). When the intrinsic wetting angle of the substrate is  $< 90^\circ$ , the apparent wetting angle and, hence, the critical nucleation work required for heterogeneous nucleation, decrease with increasing surface roughness. This decrease in the critical work facilitates oxide film generation on the surface.

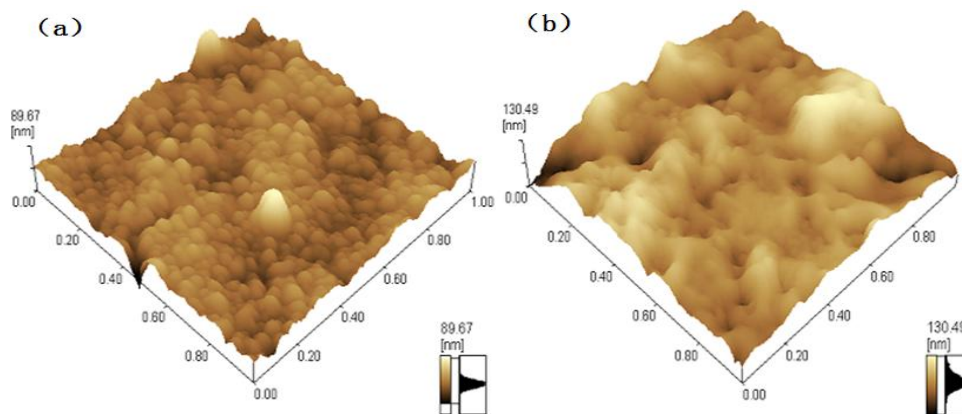


**Figure 2.** AFM Figure of (a) TA2 and (b) SMAT samples surfaces before anodization.

### 3.2 Analysis of phase composition and surface valence state of Ti and O elements

Fig. 3 shows the X-ray diffraction pattern of the TA2 and SMAT samples after anodizing. As the figure shows, the oxide film on the surface of both samples contains anatase and brookite phases of the  $\text{TiO}_2$  structure. The film thickness is less than the X-ray detection depth ( $< 35 \mu\text{m}$ ) [20] and therefore a characteristic peak corresponding to substrate Ti also occurs in the pattern. However, this peak occurs with a significantly lower intensity in the SMAT sample than in the TA2 sample. Furthermore, a diffraction peak at  $2\theta=77.38^\circ$ , corresponding to a Ti oxide, occurs for the SMAT sample. This is consistent with an increase in the thickness of the oxide film [21,22]. The considerably high diffraction peak intensities of the SMAT samples are indicative of the high crystallinity of these samples.

Fig. 4 shows the Raman spectra of the TA2 and SMAT samples. The vibration peaks in these spectra occur at Raman shifts of 153, 399<sup>1</sup>, 517, and 641  $\text{cm}^{-1}$ . This is consistent with the Raman characteristic peak reported for anatase  $\text{TiO}_2$  [23], which indicates that the anatase  $\text{TiO}_2$  structure is present in both sets of samples. The diffraction peak intensity of the SMAT sample is significantly higher than that of the TA2 sample. This indicates that the anatase  $\text{TiO}_2$  content of the SMAT sample surface is higher than that of the TA2 sample surface. We obtained the full wave at half maximum (FWHM; see Table 2) of the peaks at different positions along the Raman spectrogram. The FWHM of the anatase  $\text{TiO}_2$  peak of the SMAT sample is smaller than that of the TA2 sample. According to Bersani et al. [24], the FWHM of the Raman characteristic peak decreases with increasing crystallization. Therefore, the anatase  $\text{TiO}_2$  in the SMAT sample exhibits better crystallinity than the anatase  $\text{TiO}_2$  in the TA2 sample and the content of high-valence Ti is higher, consistent with the XRD results.

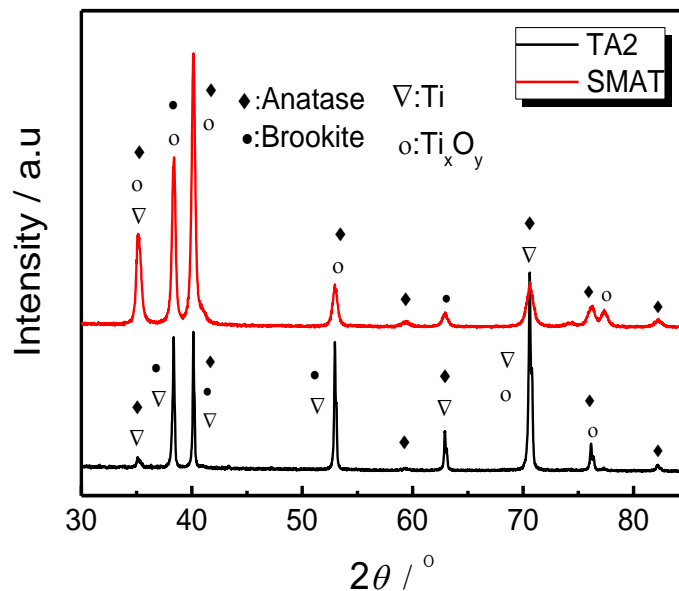


Figure 3. Phase composition of TA2 and SMAT samples.

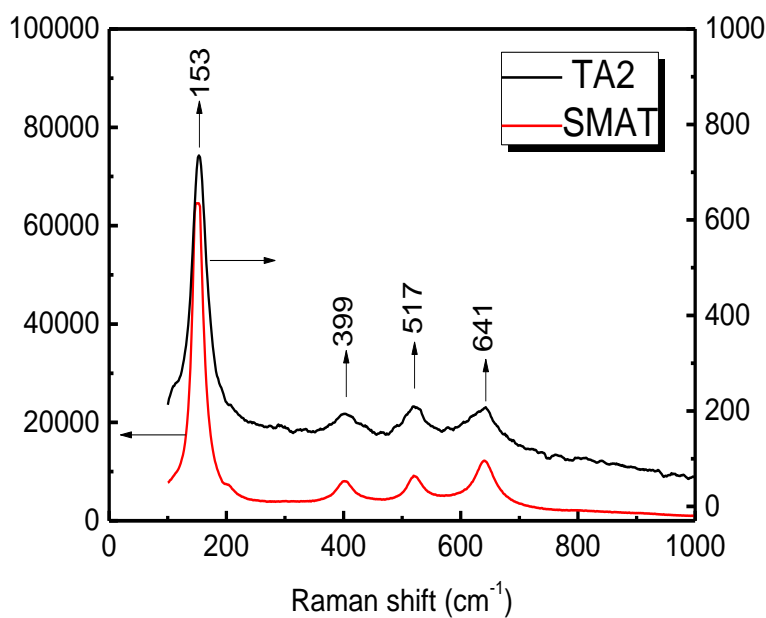


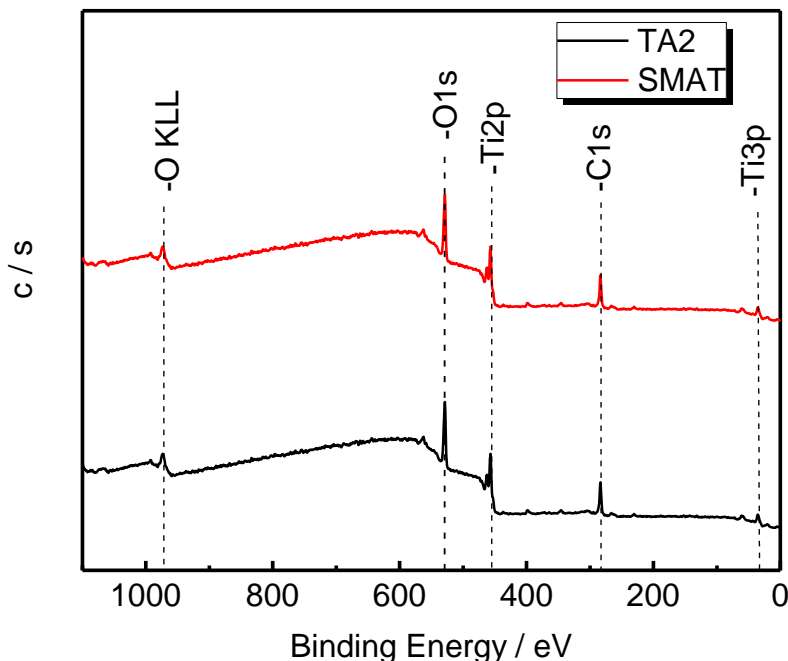
Figure 4. Raman spectrogram of TA2 and SMAT samples.

Table 2. FWHM at different positions of spectrum peak

Raman Shift / $\text{cm}^{-1}$	153	399	517	641
TA2	53.8	42.6	38.5	39.8
SMAT	47.5	27.5	27.1	34.5

Fig. 5 shows the XPS survey spectrum of the TA2 and SMAT samples. The overall spectrum shows that the oxide film on the surface of the sample is composed of elemental C (resulting from

pollution [25]), N, Ti, and O (see Table 3 for elemental content). The O content of the SMAT sample is considerably higher than that of the TA2 sample, and the excess O combines with Ti to form a new phase ( $\text{Ti}_2\text{O}_3$ ,  $\text{TiO}$ ). As the transition structure of the oxide film and the substrate, this phase can effectively improve the adhesion strength between the film and the substrate [26,27].



**Figure 5.** The XPS survey spectrum of TA2 and SMAT samples.

**Table 3.** Chemical composition of the TA2 and SMAT samples

Sample	Elemental content ( at.% , Mean $\pm$ SD )			
	C	N	O	Ti
TA2	2.13	1.01	37.36	59.13
SMAT	2.16	1.24	51.36	45.24

The valence state of the elements comprising the films are further analyzed using the narrow (i.e.,  $\text{Ti}2p$  and  $\text{O}1s$ , see Fig. 6) spectrum of the TA2 and SMAT samples. In the case of the narrow spectrum, the information depth of the photoelectron spectrum is generated from the outermost zone of the sample. The  $\text{Ti}2p$  narrow spectrum (Fig. 6[a]) of the TA2 sample consists of three pairs of overlapping peaks. The peak with binding energy at: (i)  $\text{BE}_{\text{Ti}2p_{1/2}} = 457.32$  eV,  $\text{BE}_{\text{Ti}2p_{3/2}} = 462.29$  eV represents  $\text{Ti}^{4+}$ , (ii)  $\text{BE}_{\text{Ti}2p_{1/2}} = 455.56$  eV,  $\text{BE}_{\text{Ti}2p_{3/2}} = 461.49$  eV represents  $\text{Ti}^{3+}$ , and (iii)  $\text{BE}_{\text{Ti}2p_{1/2}} = 453.89$  eV,  $\text{BE}_{\text{Ti}2p_{3/2}} = 469.87$  eV represents  $\text{Ti}^{2+}$  [28].

The  $\text{Ti}2p$  narrow spectrum (Fig. 6[b]) of the SMAT sample consists of one pair of overlapping peaks. The peak with binding energy at  $\text{BE}_{\text{Ti}2p_{1/2}} = 457.97$  eV,  $\text{BE}_{\text{Ti}2p_{3/2}} = 463.71$  eV represents  $\text{Ti}^{4+}$ , indicating that the surface oxide film is composed entirely of  $\text{Ti}^{4+}$ . During SMAT, unstable low-valence

Ti ( $Ti^{3+}$ ,  $Ti^{2+}$ ) transitions to stable high-valence Ti ( $Ti^{4+}$ ), resulting in improved stability of the oxide film, as previously indicated by the results of XRD and Raman analysis.

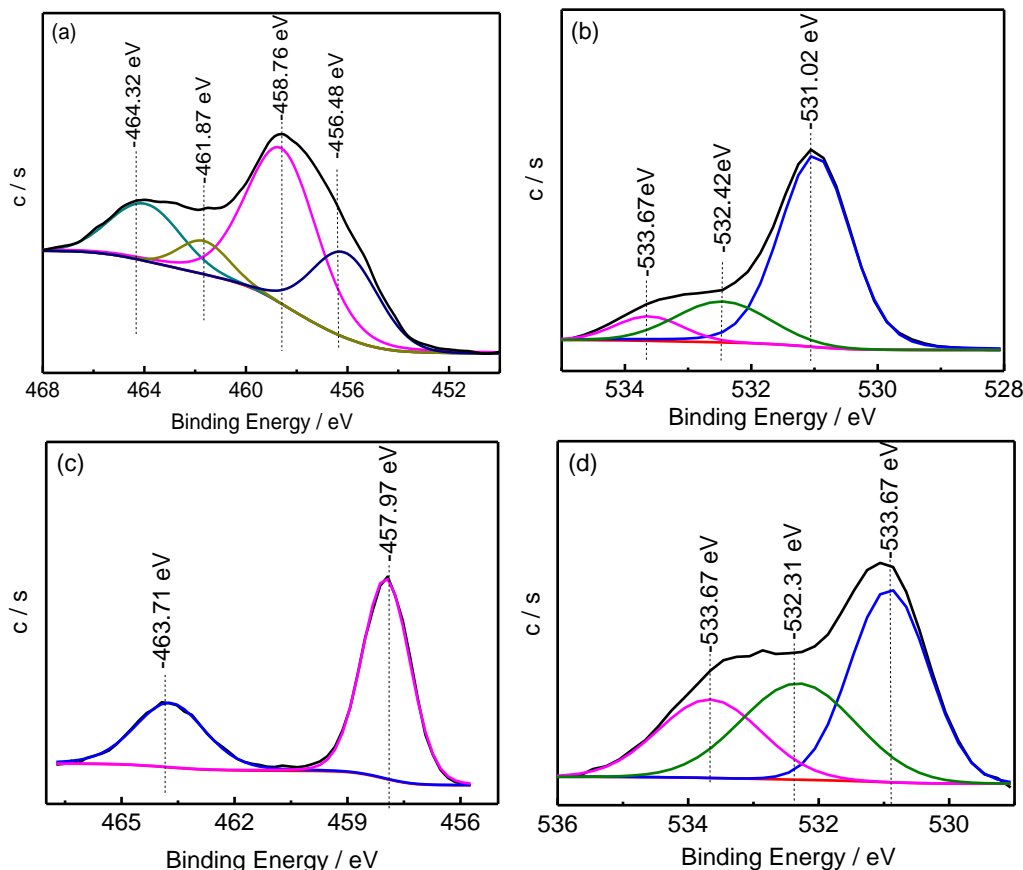


**Figure 6.** XPS spectra of (a, c) TA2 and (b, d) SMAT samples (a,b) Ti2p, (c, d) O1s

**Table 4.** Relative  $O^{2-}$ ,  $OH^-$ , and  $H_2O$  content of the oxide film formed on the TA2 and SMAT samples

Samples	Contribution of O1s components ( % )		
	$O^{2-}$	$OH^-$	$H_2O$
TA2	73.6	21.88	4.47
SMAT	77.09	17.99	3.92

The relative  $O^{2-}$ ,  $OH^-$ , and  $H_2O$  content of the oxide film (see Table 4) can be determined from the area of each overlapping peak of the O1s narrow spectrum (Fig. 6[c], [d]). The  $O^{2-}$  content of the oxide film on the SMAT sample surface is significantly higher than that of film on the TA2 sample surface, whereas the relative  $OH^-$  and  $H_2O$  content is significantly lower. Studies have shown that the formation of amorphous Ti is induced mainly by the presence of  $OH^-$  and surface bound water [29,30]. The results of the present study indicate therefore that the mechanical attrition treatment reduces the  $OH^-$  and  $H_2O$  content during anodization, and promotes the growth of the oxide film.

3.3 Corrosion resistance behavior of the film in NaCl solution

The characteristics of the passive film and the essential parameters of the electrochemical reaction process of the interface can be determined via EIS. Fig. 7 shows the Nyquist and Bode plots obtained for the TA2 and SMAT samples immersed in a 3.5 wt.% NaCl solution at 27 °C. We can see that the capacitance arc of the SMAT sample surface is larger than that of the TA2 sample surface (Fig. 7[a]). The arc reflects the charge transfer process that occurs on the electrode surface. In fact, the electron transfer resistance and the stability of the oxide film increase with increasing diameter of the arc [31]. Compared with the oxide film on the surface of the TA2 sample, the oxide film on the SMAT sample exhibits better barrier resistance against the corrosive media.

The sample surface of the TA2 and SMAT samples exhibit typical single time constants [32] (Fig. 7[b]). In high frequency regions (103–10<sup>5</sup> Hz), the phase angle increases with decreasing frequency, owing to the electrolyte reaction. Intermediate frequency regions (1–103 Hz) are characterized by an almost constant phase angle. In low frequency regions (0.01–1 Hz), the angle decreases continuously, and the characteristics of the passive film and passivation reaction are evident on the surface.

In low frequency regions, the phase angle value of the SMAT sample is considerably larger than that of the TA2 sample. Similarly, in intermediate frequency regions, the phase angle peak of the SMAT sample is significantly wider than that of the TA2 sample, and is close to 90°. Jamesh et al. [33] reported that the corrosion resistance improves with increasing phase angle. Hence, the passive film rapidly formed on the SMAT sample immersed in NaCl solution is resistant against permeation. Correspondingly, the diffusion and migration of corrosive media are hindered, and the impedance as well as the corrosion resistance are thereby improved. Therefore, the stability of the oxide film on the SMAT sample improves, charge transfer decreases, and resistance against Cl<sup>-</sup> corrosion increases with increasing phase angle.

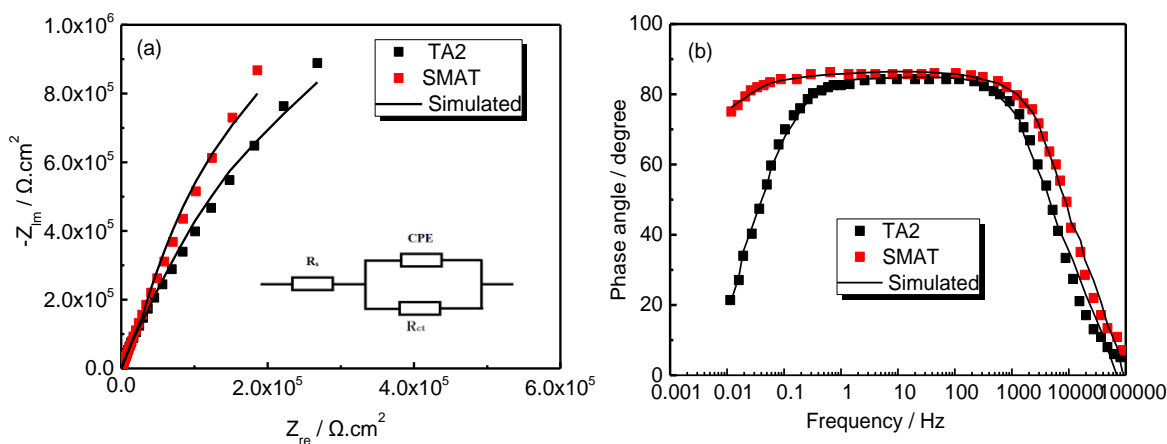


**Figure 7.** Nyquist and Bode diagrams of the (a) TA2 and (b) SMAT samples immersed in a 3.5 wt.% NaCl solution at 27 °C.

The phase angle spectrum consists of only one time constant and, hence, we have applied a fitting analysis to the surface electrochemical impedance spectrum of the sample in the 3.5 wt.% NaCl

solution. For this fitting, we have used a Randle equivalent circuit with a time constant, as illustrated in Fig. 7(a).  $R_s$ , CPE, and  $R_{ct}$  represent the solution resistance, double layer capacitance on the surface of the working electrode, charge transfer resistance of the working electrode, and diffusion resistance, respectively. The parameters of each circuit element after fitting are shown in Table 5.

**Table 5.** EIS fitting circuit parameters of the TA2 and SMAT samples immersed in a 3.5 wt.% NaCl solution

Sample	$R_s$ ( $\Omega/\text{cm}^2$ )	CPE ( $\mu\text{F}/\text{cm}^2$ )	$Z_w$ ( $\text{k}\Omega/\text{cm}^2$ )	$R_{ct}$ ( $\Omega/\text{cm}^2$ )
TA2	2.37	8.35E-3	164.7	6.35E+4
SMAT	2.5	5.76E-3	129.4	8.82E+5

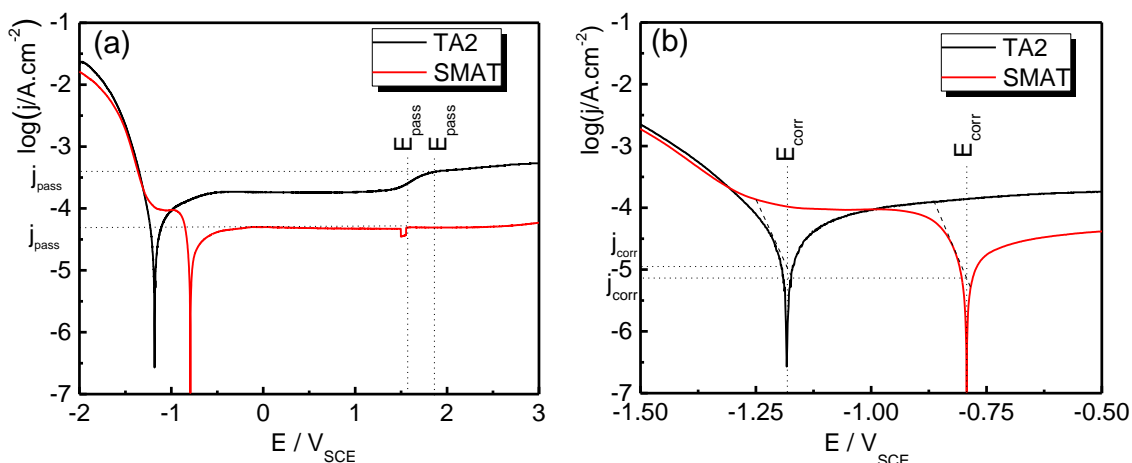
In a corrosive solution, the passive film characteristics and corrosion resistance of the material are mainly determined by the charge transfer resistance  $R_{ct}$  of the working electrode [34,35]. The corrosion resistance increases with increasing  $R_{ct}$ , and the protection efficiency of the barrier layer decreases with decreasing  $R_{ct}$ . After SMAT, the  $R_{ct}$  of the film obtained (via anodization) increases, eventually reaching a value of  $8.82 \text{ E}+5 \text{ } \Omega/\text{cm}^2$ , which is 14 times the  $R_{ct}$  of the TA2 sample. Therefore, the oxide film on the SMAT sample surface exhibits significantly higher corrosion resistance and has a better protective effect than the film on the TA2 sample.

Fig. 8 shows the potentiodynamic polarization curve of the TA2 and SMAT samples immersed in a 3.5 wt.% NaCl solution at 27 °C. Both sets of samples have undergone considerable passivation. The cathode zone of the polarization curve is characterized mainly by the occurrence of the hydrogen evolution reaction. In the anode zone, after a short dissolution, a layer of compact passive film forms on the surface of the sample, thereby resulting in passivation of the metal and inhibition of the corrosion reaction (Fig. 8[a]).

At  $E = 1.5 \text{ V}_{\text{SCE}}$ , the current density of the TA2 sample starts to increase, and the sample is further passivated. According to Olivira et al. [36], the increase in the current density (as indicated in the potentiodynamic polarization curve) reflects the breakage of the oxide film. The passivity current density maintained after re-passivation ( $j_{\text{pass}}$ ) is greater than the initial current density and increases slowly with increasing voltage. This indicates that the new passivation film is less compact than the current film. The passive film on the SMAT sample remains stable during potentiodynamic polarization testing, and the  $j_{\text{pass}}$  is significantly lower than that of the TA2 sample. This indicates that, compared with the TA2 sample, the SMAT sample is more stable in corrosive media.

Fig. 8(b) shows the Tafel zone of the potentiodynamic polarization curve. Electrochemical parameters such as the self-corrosion potential  $E_{\text{corr}}$ , self-corrosion current density  $j_{\text{corr}}$ , anodic polarization slope  $\beta_a$ , and cathodic polarization slope  $\beta_c$  [37,38] can be determined from the data in this zone (see Table 6). The  $E_{\text{corr}}$  of the SMAT sample immersed in the 3.5 wt.% NaCl solution moves 462 mV more to the positive direction than that of the TA2 sample. However, the  $i_{\text{corr}}$  decreases by  $\sim 5 \text{ mA}\cdot\text{cm}^{-1}$  indicating that, owing to SMAT, the corrosion rate and corrosion resistance of the anode oxide film decrease and increase, respectively. The hydrogen evolution reaction occurs in all zones and,

hence, the cathodic polarization slopes are relatively close. Nevertheless, the slope of the anodic polarization curve of the SMAT sample is considerably higher than that of the TA2 sample, indicating that anodic dissolution reaction of the SMAT samples is difficult.



**Figure 8.** Potentiodynamic polarization curve of the (a) TA2 and (b) SMAT samples immersed in a 3.5 wt.% NaCl solution at 27 °C.

**Table 6.** Polarization curve data of the samples immersed in a 3.5 wt.% NaCl solution

Sample	$E_{\text{corr}}/V_{\text{SCE}}$	$j_{\text{corr}}/A.cm^{-1}$	$\beta_a/ mV.dec^{-1}$	$B_c/ mV.dec^{-1}$
TA2	-0.441	0.034	110	-94.8
SMAT	-0.278	0.019	153	-95.6

#### 4. CONCLUSIONS

The SMAT process improves the roughness of the sample surface, reduces the critical nucleation work, and promotes the growth of the oxide film. After 45 min of this process, the thickness of the sample oxide film increases by 1137 nm (i.e., 3.7 times) relative to that of the pre-SMAT sample, and the compactness of the film increases. Owing to the SMAT process, the surface oxide film and the substrate forms a transition structure, thereby improving the adhesion strength of the film and the substrate. This structure promotes transformation of the low valence metastable state of Ti ( $Ti^{2+}$ ,  $Ti^{3+}$ ) to the high valence stable state ( $Ti^{4+}$ ), resulting in a stable phase structure and improved crystallinity of the oxide film.

A suitable microstructure is essential for excellent corrosion resistance. The compact structure of the oxide film on the surface of the SMAT sample yields a reduction in the density of vacancies in the film and the number of channels for  $Cl^-$  ion transmission. In a 3.5 wt.% NaCl solution, the self-corrosion potential of the TA2 and SMAT samples increases by 36.96% (from  $-0.441$  V to  $-0.278$  V) and the self-corrosion current density decreases by 44.12% (from  $0.034$   $A.cm^{-1}$  to  $0.019$   $A.cm^{-1}$ ).

Therefore, the diffusion of  $\text{Cl}^-$  ions is enhanced and the corrosion resistance of the film increases significantly after SMAT.

#### ACKNOWLEDGEMENTS

The authors are thankful for foundation support (NO 51601081 and 51665022).

We thank International Science Editing ( <http://www.internationalscienceediting.com> ) for editing this manuscript.

#### References

1. S. Yoshida, Chap., 53 (2012) 983.
2. N.X. Ya, X.X. Jing, S.X. Lan, Z.T. Feng, L. Min, Z.L. Hua, Rare. Metal. Mat. Eng., 43 (2014)241.
3. N.K. Kuromoto, R.A. Simão, G.A. Soares, Mater. Charact., 58 (2007) 114.
4. I. Milošev, D. Blejan, S. Varvara, L.M. Muresan, J. Appl. Electrochem., 43 (2013) 645.
5. L.J. Na, X.B. Shi, W.H. Dou, C.X. Fang, J. Guo, X.Z. Guo, J. Mater. Eng. Perform., 26 (2017) 1.
6. S.Z. Xue, Z.W. Zong, Adv. Mater., 20 (2008) 3663.
7. R.K. Hart, J.K. Maurin, Surf. Sci., 20 (1970) 285.
8. N.H. Fletcher, J. Chem. Phys., 29 (1958) 572.
9. M. Wang, Y. Zhang, H. Zheng, X. Lin, W. Huang, J. Mater. Sci. Technol., 28 (2012) 1169.
10. F.T. Lin, Z.Z. Lin, Z. Ling, T. Mater. Heat. Treat., 35 (2014) 207.
11. Y.X. Hua, Z.Z. Lin, R. Ju, L. Zhong, L. Li, L.J. Xiong, Chem. Phys. Lett., 600 (2014) 43.
12. Y.X. Hua, R. Ju, Z.Z. Lin, L. Zhong, L.J. Xiong, Mater. Design., 83 (2015) 159.
13. F.T. Lin, W. Xiao, L.J. Xiong, L. Li, Y.X. Hua, Z.Z. Lin, JOM., 69 (2017) 1844.
14. Y.X. Hua, Z.Z. Lin, *Nanoscale. Res. Lett.*,9 (2014) 516.
15. F.T. Lin, Z.Z. Lin, Z. Ling, *T. Mater. Heat. Treat.*, 35 (2014) 207.
16. R.N. Wenzel. *Ind. Eng. Chem.*, 28 (1936) 988.
17. W. Jing, M.X. Cai, W.Y. Hong, M. Ying, L. Ting, S.W. Li, *Rare. Metal. Mat. Eng.*, 42 (2013) 491.
18. M. Nakamura, L. Sirghi, T. Aoki, Y. Hatanaka, *Surf. Sci.*, 507 (2002) 778.
19. C. Qi, L. Cheng, M. Kun, Y.X. Hua, Z.Y. Nan, L.J. Xiong, J. Xin, J.L. Ying. *Int. J. Electrochem. Sci.*, 13 (2018) 265.
20. H.X. Wen, L.Z. Jian. *Surf. Coat. Tech.*, 232 (2013) 224.
21. B.J. Wei, Z.X. Tao, W.Z. Guo, H.X. Quan, L.Y. Ling, F.X. Dong, *J. Sichuan. Univ. Nat. Sci. Ed.*, 41 (2004) 995.
22. W. Xiao, R. Ju, S.Y. Min, Y.X. Hua, Z.Z. Lin, D.J. Shuai, *Phys. Leyy. A.*, 381 (2017) 2845.
23. L.D. Arsov, C. Kormann, W. Plieth, *J. Raman. Spectrosc.*, 22 (1991) 573.
24. D. Bersani, P.P. Lottici, X.Z. Ding. *Appl. Phys. Lett.*, 72 (1998) 73.
25. W. Xiao, Z.Y. Nan, L. Cheng, Y.Z. Tao, Z. Yi, Z.Z. Lin. *Int. J. Electrochem. Sci.*, 12 (2017) 12009.
26. W.Z. Guo, X. Cai, C.Q. Long, C. Paul, *Thin. Solid. Films.*, 515 (2007) 3146.
27. C.S. Tian, G. B, W. Yu, P.J. Hong, *Mater. Sci. Tech.*, 24 (2016) 82.
28. H. Satoshi, T. Akihiro. *Surf. Interface Anal.*, 34 (2010) 262.
29. X.Z. Bin, N. Hiroshi, T. Hiroyuki, E. Takeo, I. Miki, F. Motoaki, O. Jun, *Electrochem. Commun.*, 9 (2007) 850.
30. B.J. Hwang, J.R Hwang, *J. Appl. Electrochem.*, 23 (1993) 1056.
31. M.A. Khan, R.L. Williams, D.F. Williams, *Biomater.*, 20 (1999) 631.
32. M. Fazel, H.R. Salimijazi, M.A. Golozar, H.M. Garsivaz jazi, *Appl. Surf. Sci.*, 324 (2015) 751.
33. J.M. Ibrahim, L. Penghui, B. Marcela, R.L. Boxman, M. David R. *Corros. Sci.*, 97 (2015) 126.
34. R. Ju, Y.X. Hua, Z.Y. Nan, *Int. J. Electrochem. Sci.*, 12 (2017) 11987.
35. E.M. Szesz, C.E.B. Marino, H.A. Ponte, F.C.N. Borges. *Key. Eng. Mater.*, 396 (2009) 381.

36. N.T.C. Oliveira, A.C. Guastaldi. *Acta. Biomater.*, 5 (2009) 399.
37. S.L.D. Assis, S. Wolyneć, I. Costa. *Electrochim. Acta.*, 51 (2006) 1815.
38. W.G. Song, D.K. Jian, Z.X. Qing, W.X. Min, Y.S. Shan. *Scripta. Mater.*, 61 (2009) 269.

© 2018 The Authors. Published by ESG ([www.electrochemsci.org](http://www.electrochemsci.org)). This article is an open access article distributed under the terms and conditions of the Creative Commons Attribution license (<http://creativecommons.org/licenses/by/4.0/>).